Fatigue crack initiation in the presence of stratified surface layers on rail wheels

M. Freisinger [a,c,*], B. Jakab [a], K. Pichelbauer [a], G. Trummer [b], K. Six [b], P.H. Mayrhofer [c]

[a] *AC2T Research GmbH, A-2700 Wiener Neustadt, Austria*
[b] *Virtual Vehicle Research Center, A-8010 Graz, Austria*
[c] *Institute of Materials Science and Technology, TU Wien, A-1060 Wien, Austria*

ARTICLE INFO

ABSTRACT

This work presents a study on the fatigue crack initiation in the presence of stratified surface layers (SSL) – a combination of white and brown etching layer – on rail wheels. Reproducible SSLs comparable to field samples are created by a defined mechanical load and two consecutive laser surface treatments on discs made from two wheel materials (ER7, ER9). Fatigue testing is done by a twin disc tribometer, where the wheel discs with SSLs are driven against discs made from R260 rail material. The results show significant fatigue crack initiation and propagation in the presence of the SSLs, exclusively on the leading edge of the SSL, more pronounced for the wheel grade ER9. Based on topographical, light optical and scanning electron microscopy analysis an explanatory model is presented, describing fatigue crack morphologies and outpointing the relevance of SSLs on rail wheels to fatigue crack initiation.

1. Introduction

In order to meet the worldwide climate targets, public transportation gains in significance in recent years, especially rail traffic. Higher train frequency increases load on rail and wheel materials. Thus, for further guaranteed safety and reliability in railway transportations, understanding the most dominating damaging mechanisms of rail and wheel materials is crucial. Additionally, maintenance costs can be reduced by clarifying the interaction of certain mechanical and thermal loads, materials, and their failure mechanisms. Therefore, the number of published investigations of rail and wheel defects increased and also a more sophisticated terminology developed [1-6]. Regarding rails, two types of apparently similar looking defects are discussed in recent literature, namely the squat defect and the stud defect [1,7-9]. Squat defects – a result of rolling contact fatigue (RCF) – originate from plastic deformation [10], while stud defects are stated to originate from brittle white etching layers (WEL) [11]. The latter is named after its white appearance during light optical microscopy (LOM) when etching with an ethanol nitric acid. This layer forms either mechanically by severe plastic deformation (SPD) or thermally by increased temperature and rapid cooling [12-15]. In rolling-sliding contacts, the WEL frequently contains a martensitic microstructure with hardness values of 700 – 1000 HV and

fracture toughness values of approximately 15 MPa m$^{1/2}$, which lead to a brittle behavior [13,16-18]. In terms of RCF damage related to WELs, studies have been predominantly presented on rails from service [19-22]. We envision that squat and stud related defects also play important roles for wheels. Especially the RCF clusters in the center of wheel treads show similarities to squat and stud defects [23]. The WELs formed on wheel surfaces – due to extensive slipping and braking [3,24-26] – have their impact on the formation of RCF clusters. For rails, Farjoo et al. [19] suggest the relation of WEL to squat formation and give results of finite element modeling to point out that a short crack in the WEL increases the bending stress and peak effective stress intensity factors. This consequently leads to a higher crack growth rate. Seo et al. [22] investigated the fatigue life of rail samples with WELs simulated by wheel flats. The authors show that the highest risk of RCF occurs at the leading edge of the WEL. Lian et al. [20] applied a finite element modeling with elastic plastic as well as linear elastic fracture mechanics theory and present similar results. Under the same loading conditions, the cracks initiating at the leading edge of the WEL show the most likely growing tendency. However, various influences such as material properties, sample geometry or axle loads are mentioned. By now, no studies on wheel materials are known by the authors, moreover, most studies are limited due to the uncertain loading history of the samples from the

---

* Corresponding author.
E-mail address: matthias.freisinger@ac2t.at (M. Freisinger).

field.

In addition to the WEL, increasing attention is paid to another important, modified surface-near region – the so-called brown etching layer (BEL) [27-30]. Earlier studies by Ahlström et al. [31] mentioned this as tempered martensite. Later, Li et al. [27] named the frequently formed sublayers of WELs due to their brownish appearance during metallographic studies as BEL, which is significantly softer than the WEL. They also proposed that BELs are formed by repeated martensite-austenite-martensite transformations, leading to tempered martensite (in agreement with Ahlström et al. [31]). A clear formation mechanism could not be given, as the loading profiles of field samples are unknown. But they additionally stated that the BEL reveals an increased risk to RCF, because cracks propagate deeper into the material than observed for WELs. Messaadi and Steenbergen [30] named the combination of WEL and underlying BEL as stratified surface layer (SSL) and concluded that the BEL – being a globular bainitic microstructure and formed by a thermomechanical loading cycle – contributes to the development of RCF. The wheel–rail contact situation during operation leads to temperatures and loading profiles sufficient for austenitization of their near-surface regions. The different cooling rates in different surface-regions causes the formation of various microstructures.

Kumar et al. [28] extended the formation mechanisms for BELs based on investigating a curved rail track (with unknown loading history, as typical for field samples) and came to the conclusions that the multiple cycles of severe plastic deformation and loading combined with the increased temperature (upon loading) cause a modification of the pearlitic microstructure in near-surface regions where the temperature was too low for austenitization. The cementite laths of pearlite are fragmented and partially dissolved, as a finer microstructure allows for a higher C content in the alpha regions [32]. Regions experiencing a temperature sufficient for austenitization contain a high fraction of martensite, which under certain wheel–rail contact conditions or for certain temperature-profiles (due to specific regions in the wheel or rail) are tempered to precipitate secondary carbides, forming the BEL. The gaining interest on BELs underneath WELs and extensive studies on their microstructural characteristics suggest a possible influence on RCF damage. Besides analysis of samples from the field, systematic studies are needed to clarify the effect of underlying BELs to RCF crack initiation and growth of rail and wheel materials.

Hence, this paper presents a novel experimental procedure to investigate fatigue crack initiation in the presence of SSLs (WELs + BELs) in wheel materials. A laboratory approach to create SSLs with defined loading history (mechanical and thermal loadings) is introduced to eliminate the uncertainty due to unknown loading histories of samples from field. Mechanical loads are applied by using a twin disc tribometer, followed by defined thermal loads via laser surface treatments. This approach shows good comparability to field samples and paving the way to study fatigue crack initiation of SSLs under defined and reproducible conditions. Based on tribometer tests with following topographical and microscopical analysis an explanatory model for the fatigue crack initiation in the presence of SSL on rail wheels is presented. This improves the understanding of RCF failures caused by SSL, leading to unplanned maintenance and therefore decreased capacity and delays of rail transportation systems.

2. Materials and methods

Two wheel materials with different carbon content (grades ER7 and ER9), and one rail material (grade R260) – Table 1 summarizes chemical and mechanical details of these commonly used materials on European rail networks – are used as base material for further treatments and investigations. From the heads and the crown of the rail and wheel, provided by the Austrian Federal Railways (ÖBB), specimens (original 60x60x15 mm^3) were cut out. The end faces of the discs are parallel to the running track of the wheel or rail. Still in their cut-out cuboid shape, the samples were heat treated (homogeneous austenitization in a chamber furnace for 30 min at 900 °C followed by quenching in oil and tempering for 60 min at 510 °C followed by cooling in ambient air) to achieve a microstructure comparable to the original near-surface microstructure of an as-manufactured wheel and rail. For the wheel materials, a pearlitic microstructure with pro-eutectoid ferrite is achieved with a bulk hardness of ~300 HV (ER7) and ~330 HV (ER9). The rail discs show a pearlitic microstructure and a hardness of ~260 HV. After heat treatment, the specimens where machined to their final disc dimensions (Fig. 1).

In a previous study [14], we showed that for a representative lab-produced WEL (via laser treatments) on wheel materials a pre-deformed state is crucial. Otherwise, the lab-produced WEL significantly deviates in its microcharacteristics from the field-generated WEL on rails or wheels. While in the previous study we used a pre-deformed material from field (naturally without a deep knowledge of the loading history), here we introduce a combination of a twin disc tribometer and a diode laser system to allow for a well-defined mechanical and thermal loading profile. After the mechanical loading (mechanical load M1) under controlled conditions (Fig. 1) followed the laser treatment (thermal load T1 and T2) via a Direct Diode Laser System (HighLight 8000D, Coherent, U.S.). This novel laboratory approach is schematically shown in Fig. 2. Within the customized twin disc tribometer, two discs (diameter: 50 ± 2 mm, thickness: 10 mm) roll against each other while being pressed together with a defined normal load of 800 N (Hertzian pressure of 766 MPa). The driving disc is made of the wheel material, and the driven disc is made of the rail material. Both speeds (ω_W for wheel and ω_R for rail) can be controlled individually and continuously, allowing to control the resulting slip, s, according to:

$$s = \frac{2*(\omega_W - \omega_R)}{\omega_W + \omega_R} \quad (1)$$

The tests were conducted at room temperature, without intermediate medium (dry), with $\omega_W = 500$ rpm and a slip of $s = +1\%$, for 100,000 cycles.

Table 1
Chemical composition and mechanical properties of the steel grades ER7, ER9 and R260 according to the standard EN13262 [33] and [34], fracture toughness K_Q value obtained by compact tension specimens [35].

	C	Si	Mn	P	S	Cr	Cu	Mo	Ni	V	Cr + Mo + Ni
	[wt%]										
ER7	0.52	0.40	0.80	0.020	0.015	0.30	0.30	0.08	0.30	0.06	0.50
ER9	0.60	0.40	0.80	0.020	0.015	0.30	0.30	0.08	0.30	0.06	0.50
R260	0.74	0.31	1.08	0.013	0.018	0.040	–	–	–	–	–

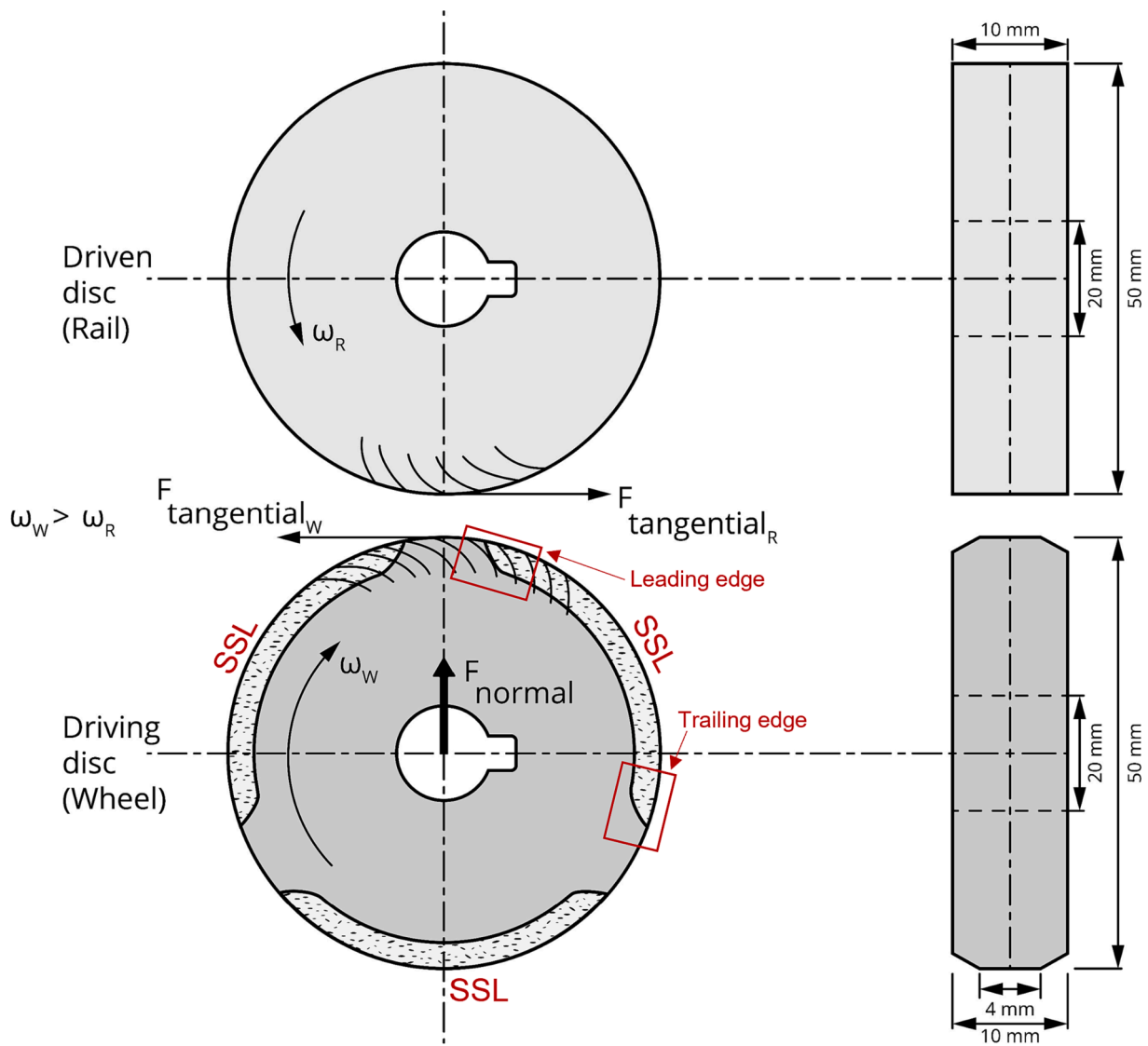|	R_{eH}		R_m		A_5		Minimum Hardness			K_Q	
	[N/mm^2]		[N/mm^2]		[%]		[HB]			[MPa m$^{1/2}$]	
ER7	≥520		820–940		≥14		235			40–80	
ER9	≥580		900–1050		≥12		255			–	
R260	528		923		11.4		260			–	

Fig. 1. The configuration of the twin disc tribometer used for the initial mechanical loading before the thermal loadings, and for the fatigue testing of the created SSLs. The driving disc (wheel material, grade ER7/ER9) is pressed with a normal load F_{normal} towards the driven disc (rail material, grade R260). The wheel samples for the fatigue testing feature three SSL sections, whereby the leading edge of the SSL is named side A and the trailing edge side B.
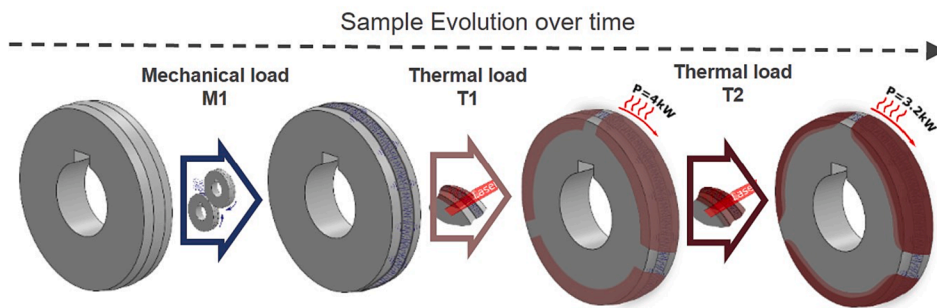

Fig. 2. Approach to imitate reproducible SSLs with defined loading history: In the first step, the material is mechanically deformed by a twin disc tribometer run (M1), followed by two thermal loads with different laser energy powers in three distinctive regions of the sample (T1: P = 4.0 kW, T2: P = 3.2 kW).

The following laser treatments are conducted with a rectangular laser spot (3 mm in moving direction and 36 mm perpendicular to it), a nominal continuous power output of 8 kW at a wavelength of 975 nm. The laser system (mounted on a 6-axis robot arm (IRB 4600–60/2.05, ABB, Austria) and controlled via the teach-pedant of the controller system of the IRC5 (ABB, Austria)) can precisely be positioning and moved. The starting temperature of the surface for each laser-treated track was room temperature, and along the circumference of the discs three sections were treated by moving the laser spot with a constant speed of 12 mm/s, Fig. 1 and Fig. 2. Pre-studies showed that for a field-

near development of the SSL a double-laser treatment is needed, with an initial laser power (T1) of 4.0 kW followed by 3.2 kW (T2). Between the laser treatments a cooling to room temperature of the samples was guaranteed.

To introduce RCF cracks, the prepared wheel disc samples (ER7, ER9) with three SSL sections along the tread surface were run against rail material discs (R260). Same loading parameters are applied as used initially ($F_N = 800$ N, 500 rpm, s = +1%, 100,000 cycles).

The tested samples were characterized with a focus-variation microscope (Alicona InfiniteFocus G5, Alicona Imaging GmbH, Austria) for their surface topography. After metallographic sample preparation of cross-sections to a mirror-polished surface quality (1 μm diamond fine polishing), their surfaces were etched with diluted nitric acid (3% HNO_3, 97% ethanol) and analyzed via light optical microscopy (LOM, Axio Imager M2m, Carl Zeiss AG, Germany) and field emission gun scanning electron microscopy (SEM, Jeol JIB 4700F, Jeol Ltd., Japan) operated at 15 kV acceleration voltage using secondary electron (SE) and backscattered electron (BE) mode. Certain regions of the samples were characterized for their low load Vickers hardness using a Future-Tech FM-700 hardness tester (Future Tech Corp., Japan) with a load of 0.01 kp (0.098 N).

3. Results

3.1. Formation of SSL with defined mechanical and thermal loads

Combining a twin disc tribometer with a diode laser system allows the imitation of a SSL with distinctive regions of WEL and BEL, see Fig. 3 and Fig. 4, respectively. The initial mechanical load (M1) by the twin disc tribometer leads to an SPD near-surface microstructure (SPD-ER7) within a distance of ~200 μm from surface, see the cross-sectional cuts of a representative SSL on ER7 wheel material given in Fig. 3a and b. The following laser treatments cause thermal loads (T1, T2) leading to the formation of an SSL with an average thickness of ~500 μm. The transition zones along the surface (SPD-ER7 – BEL – WEL) shows no severe cracking due to residual stresses within the treated regions.

Within the SSL, a WEL and BEL region can be identified, where the WEL comes up with an average thickness of ~350 μm. The martensitic microstructure in various depths from surface can be seen through BE and SE images, Fig. 3c and d (50 μm), Fig. 3e and f (100 μm), and Fig. 3g and h (250 μm), respectively. Even though the initial degree of deformation of the ER7 wheel material before the thermal loads (Fig. 3i–n) is different, no significant difference in the martensitic microstructure can be identified. The BE image of the SPD-ER7 microstructure in a depth of
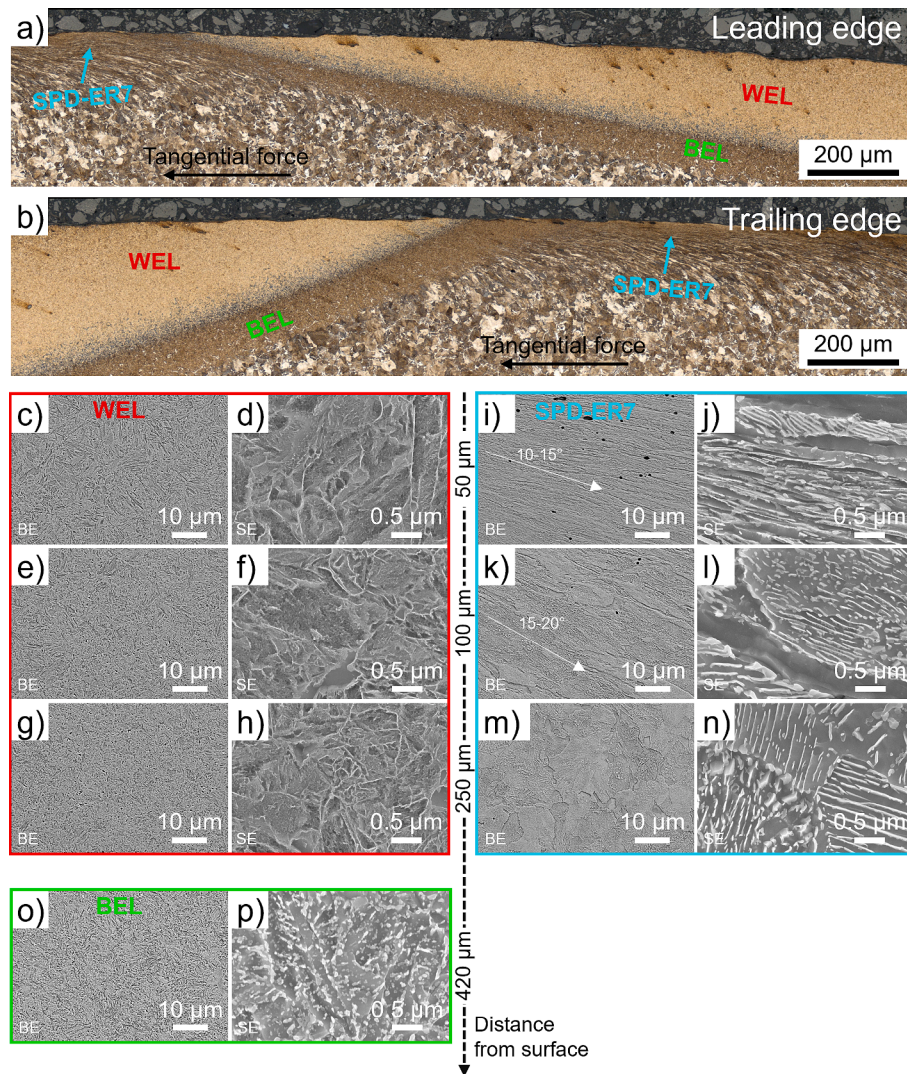

Fig. 3. (a), (b): LOM images of the transition regions showing the initial ER7 microstructure deformed by mechanical loading (M1) (SPD-ER7) and the thermally induced SSL consisting of the WEL and BEL. Detailed BE and SE images in various depths from surface are presented for the WEL ((c)–(h)), the SPD-ER7 ((i)–(n)) and the BEL ((o),(p)).
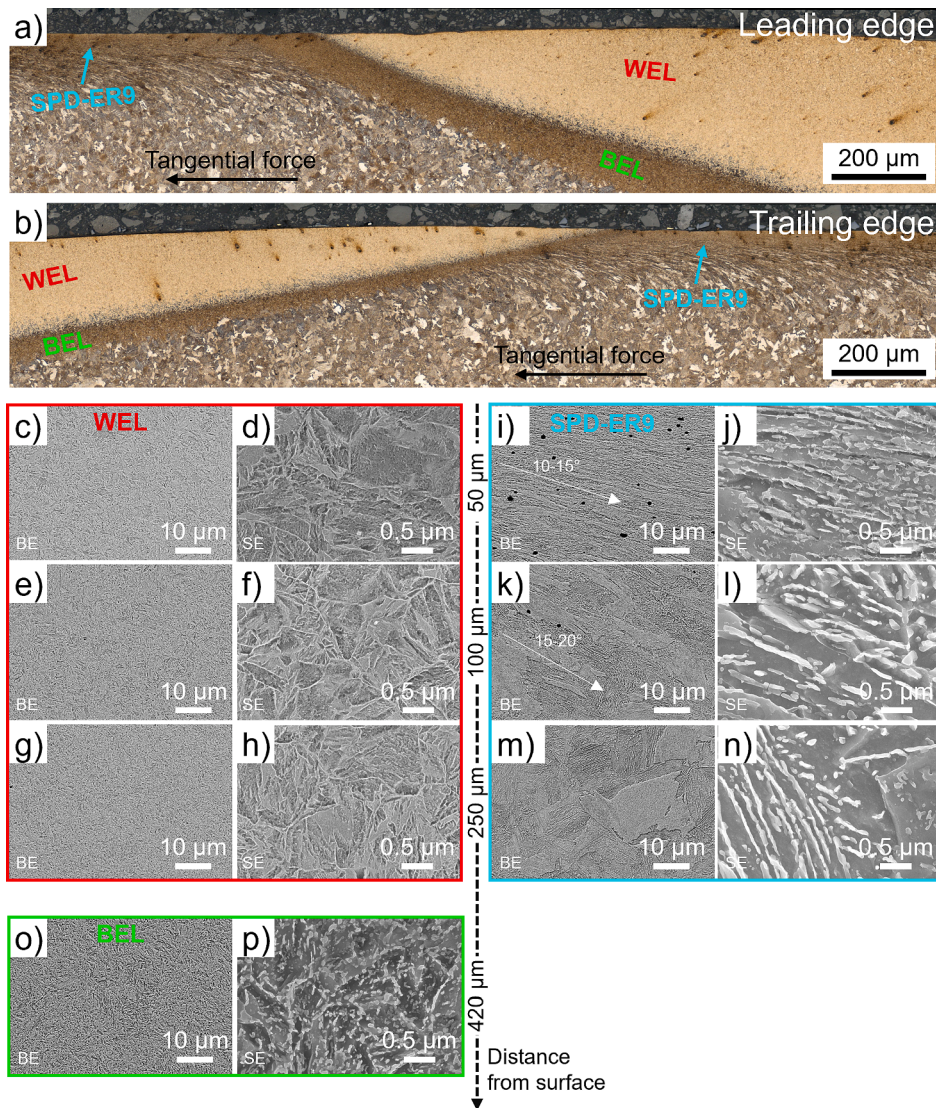
Fig. 4. (a), (b): LOM images of the transition regions showing the initial ER9 microstructure deformed by mechanical loading (M1) (SPD-ER9) and the thermally induced SSL consisting of the WEL and BEL. Detailed BE and SE images in various depths from surface are presented for the WEL ((c)–(h)), the SPD-ER9 ((i)–(n)) and the BEL ((o),(p)).

50 μm from surface (Fig. 3i) shows an SPD microstructure with an alignment of 10–15° to the surface. The higher magnification SE image (Fig. 3j) indicates deformation, fracture, and alignment of the cementite lamellae. In a depth of 100 μm from the surface (Fig. 3k and l) the degree of deformation is decreasing, and the alignment angle is increasing (15–20°). An undeformed ferritic-pearlitic microstructure can be identified in a depth of 250 μm from the surface (Fig. 3m and n). The BEL region of the SSL can be clearly seen due to its brownish appearing microstructure in the LOM images (Fig. 3a and b) and reveals a thickness of ~150 μm. Analysis of the microstructure in the middle of the BEL region (420 μm from surface) indicates a trend for an increased grain size (Fig. 3o) in comparison with the WEL microstructure, and the SE image (Fig. 3p) shows a proceeded cementite spheroidization (Fig. 3o).

Images of the cross-sectional cuts after the initial mechanical loading (M1) and followed thermal loads (T1, T2) for the wheel grade ER9 are given in Fig. 4. Comparable SSLs (WEL + BEL) with thicknesses of ~510 μm on an initially deformed microstructure (SPD-ER9) and crack-free transitions are present (Fig. 4a and b). The BE and SE images of the WEL region (Fig. 4c–h) show a martensitic microstructure without significant differences for the presented depths from the surface (50, 100, and 250 μm). Fig. 4i–n show the related initial ER9 microstructure

before the thermal loads. Deformed and fractured cementite lamellae can be identified, with an alignment angle of 10–15° in a depth of 50 μm and 15–20° to the surface in a depth of 100 μm. In a depth of 250 μm from surface the ER9 microstructure is mechanically unaffected. The brownish appearing BEL region within the LOM images comes up with an average thickness of 140 μm and a tempered martensite microstructure (Fig. 4o and p) with globular cementite particles due to spheroidization during the second thermal load (T2).

3.2. Fatigue testing of SSLs on rail wheel materials

The defined SSLs created by mechanical and thermal loads (M1, T1 and T2) are further treated by another mechanical load (M2) applied by the twin disc tribometer, which mimics the wheel–rail contact in service. Being most critical in terms of crack initiation, the transition regions are the focus when analyzing the specimens.

Fig. 5 shows LOM images of cross-sectional cuts in the transition zones of the SSLs to the deformed ER7 base material after 100,000 cycles under defined twin disc tribometer parameters (M2). Six thermal loaded zones are analyzed, significant differences in material behavior for the leading edge and the trailing edge of the SSL can be seen: 3 out of 6
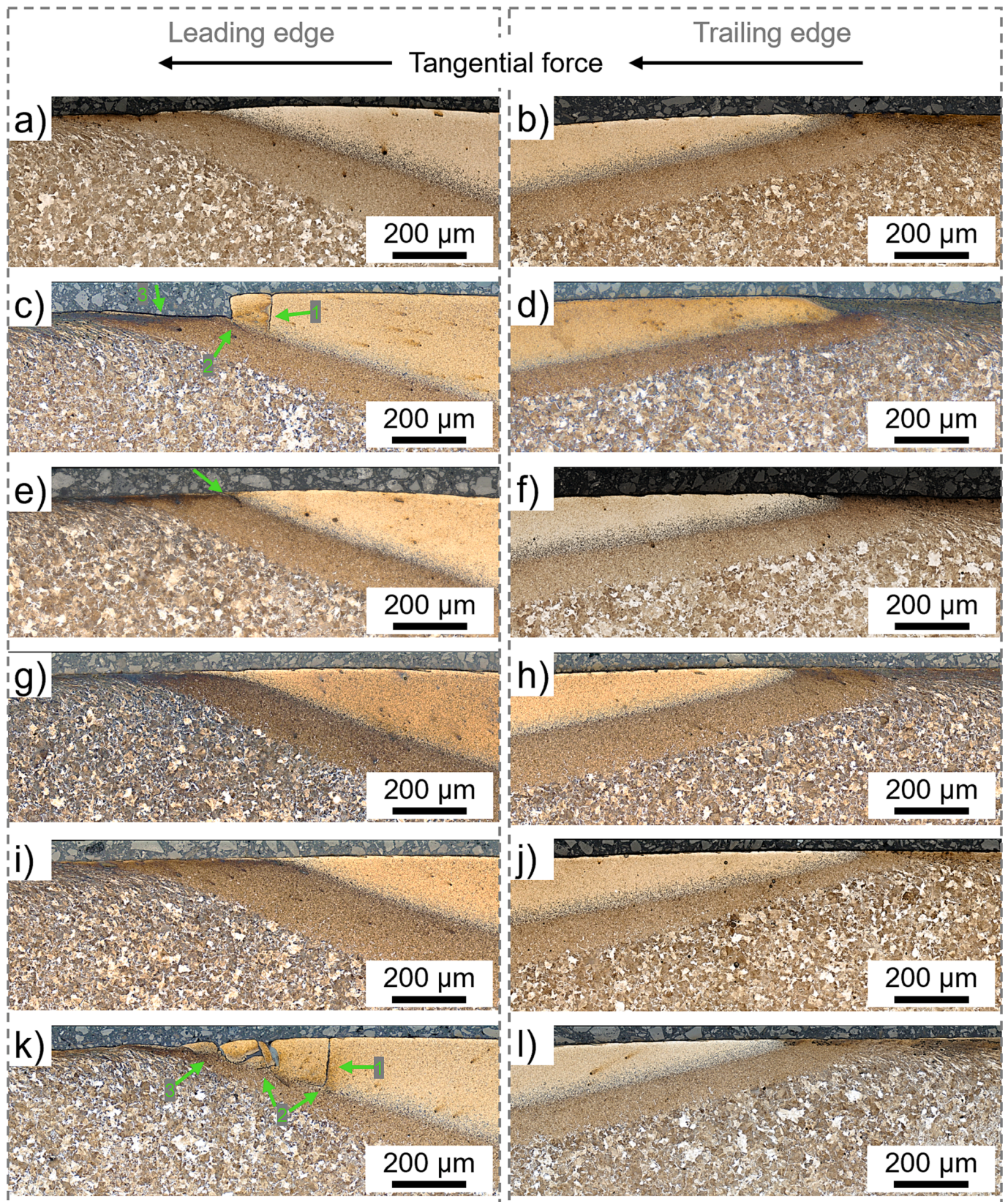
Fig. 5. LOM images of the transition zones from base material to SSLs in cross-sectional cuts for wheel material ER7. The leading edges of the SSLs show failure patterns for 3/6 transition zones: Crack initiation and propagation under 90° to surface within the WEL (1), branching at the WEL/BEL interface (2), and deformation of the BEL due to WEL fragments (3). For the trailing edges of the SSLs, no cracking patterns are detected, but plastic material flow of the base material over the WEL region.

transition zones at the leading edge showed no crack initiation (Fig. 5a, g and i). Within the BEL and WEL transition regions, plastic deformations are present with shallow cracks and small spallation events along the WEL surface. The other transition zones at the leading edge of the SSL show different stages of crack propagation and failure. Fig. 5e captures a crack within the BEL/WEL interface at the disc surface along the plastically deformed microstructure, but no significant crack propagation into the depth is present. More severe cracking is presented in the region captured by Fig. 5k, which shows multiple cracks propagating under ~90° to the surface within the WEL region (Fig. 5k: 1). At the interface to the BEL, the cracks branch (Fig. 5k: 2). One crack-branch propagates in the direction of the tangential force along the WEL/BEL interface. Another crack-branch propagates in the other direction under a certain angle into the BEL. Joining of these cracks seems to result in WEL fragments, which are pushed against the underlying BEL due to the tangential and normal forces, leading to an SPD of the BEL (Fig. 5k: 3). A similar failure mechanism seems to be present in the region given in Fig. 5c, but the WEL fragments for this region are already spalled. The crack tip of the visible crack propagating under ~90° into the WEL is just in front of the WEL/BEL interface, hence, no branching can be seen in this case (Fig. 5c: 1). At the edge of the spalled WEL region a branched crack, propagating under a certain angle into the BEL region, is present (Fig. 5c: 2). This indicates a higher crack growth rate for cracks propagating along the WEL/BEL interface in the direction of the tangential force. At the region of the spalled WEL fragments, the BEL shows severe deformation (Fig. 5c: 3).

Regarding the trailing edges of the SSLs, where the tangential force points from the base material to the SSL, no cracking is observed (Fig. 5b, d, f, h, j, l). In contrast, there is major plastic deformation, and the ER7 material respectively the BEL seems to be pulled over the WEL to a certain degree. This is impressively present in the region captured by Fig. 5d, where the tangential forces plastically deform the ER7 material over the WEL region.

A focus-variation microscope allows to extract additional information from these transition regions, Fig. 6. A smaller wear track is present in the grey blue appearing region, where the thermal loads have formed an SSL. The leading edges of the SSLs (Fig. 6a, c, e, g, i, k) show some areas, where small regions spalled within the SSL, clearly visible in Fig. 6a. At the transition zone of the deformed ER7 material and the SSL, cracks (Fig. 6c: 1), but also spallation (Fig. 6c: 2) within the SSL next to the transition region are present. Within the transition region pictured in Fig. 6k (referring to cross-section Fig. 5k) massive crack patterns formed (Fig. 6k: 1) and also spallation of some parts at the transition zone occurred (Fig. 6k: 2). The trailing edges of the SSLs (Fig. 6b, d, f, h, j, l) do not show significant damage patterns. Within the ER7 wear track, oxide lamella, adhered debris and ploughing features are present.

In the transition zones of the SSLs to the base material ER9 after twin disc tribometer testing, fatigue cracks are present in 4 out of 5 transition zones at the leading edge of the SSLs, see the LOM images of the cross-sectional cuts given in Fig. 7a, c, e, g, i. The damage patterns exhibit similar characteristics to those of the ER7 discs (Fig. 5) but more severe. The crack propagating ~90° to the surface within the WEL region, Fig. 7e, is a sign of the first stage of fatigue damage of the SSLs. The tip of the crack (which seems to have no branching) is just before the WEL/BEL interface. Within the transition zone multiple cracks perpendicular to the surface formed (Fig. 7c: 1), which branch at the WEL/BEL interface (Fig. 7c: 2). As described for the ER7 wheel material, one crack branch propagates along the WEL/BEL interface in the direction of the tangential force, while the other propagates under a certain angle into the BEL in opposite direction. In addition, there is severe deformation of the BEL and an almost loose WEL fragment (Fig. 7c: 3). The features present in the transition zone indicate an already proceeded stage where the initial cracks within the WEL (Fig. 7g: 1) branched at the WEL/BEL interface (Fig. 7g:2). Subsequent joining of the cracks leads to the formation of WEL fragments, followed by a deformation of the underlying BEL (Fig. 7g: 3). Similar characteristics are present in the regions shown

in Fig. 7i. There, the WEL fragments already spalled, and a massive pit is formed. The LOM images for the trailing edge of the SSLs (Fig. 7b, d, f, h, j) show no crack initiation at the transition zone, but plastic deformation and material flow in direction of the tangential force with some amount of material plastically deformed over the SSL.

As for the ER7 discs, the wear track along the grey-blue appearing region (SSL) is significantly smaller, see the surface images of the tested ER9 discs, Fig. 8. Radial cracks origin from the transition from the ER9 base material to the SSL extend throughout the SSL at the leading edge (Fig. 8a, c, e, g, i). This is impressively shown in Fig. 8c: 1 (the corresponding cross section is given in Fig. 7c), which regularly cause the spallation of large areas (labelled with 2 in Fig. 8c). Corresponding characteristics are present in the region captured by Fig. 8g (the corresponding cross-section is Fig. 7g) and in a more severe stage in the region shown by Fig. 8i (the corresponding cross-section is Fig. 7i). Radial cracks but no spallation is present in the region presented in Fig. 8e (the corresponding cross-section is Fig. 7e). As for the ER7 discs, there is no severe damage in the transition regions of the trailing edge (Fig. 8b, d, f, h, j). Within the wear track, oxide lamella and adhered debris are present, with some amount of ploughing. This is more significant within the wear track of the ER9 base material.

3.3. Explanatory model of fatigue crack initiation of SSLs on rail wheel materials

Based on the results of the twin disc tribometer tests, presented in the previous section, the fatigue crack initiation and propagation within SSLs on wheel materials can be divided into different stages. With the help of in-depth SEM investigations of representative ER7 and ER9 samples, an explanatory model was derived, featuring various stages:

The first stage (*Stage I*) is characterized by a dominating gradual wear without crack formation in the transition zone of the SSL to the deformed wheel base material (Fig. 9a). At this stage, the mechanical load of the twin disc tribometer caused plastic deformation and detachments of wear debris. For the wheel material, the deformation is obvious down to ~200 μm from the surface, as described above (Figs. 3 and 4). Besides its hard and brittle nature, the WEL of the SSL shows plastic deformation down to ~10 μm from the surface with aligned martensite grains (increasing angle to the surface with increasing depth (Fig. 9b)). The WEL region exhibits micro-cracks, which shallowly propagate at an angle of 10 – 15° to the surface. At a certain point, the cracks tend to grow towards the surface leading to the formation of small, detached particles (Fig. 9c and d). This cracking mechanism is present along the WEL surface of the whole disc and is not related to the transition zones. It is the result of wear-related micro-crack formations, which are also present in regions without SSLs. However, no macroscopic cracks are formed and hence, no critical fatigue crack initiation takes place at this stage.

In the next stage, named *Stage II*, significant macroscopic crack initiation is evident within the WEL at the leading edge of the SSL (Fig. 10a). Out of several micro-cracks initiated in *Stage I*, certain conditions lead to a crack propagating along the alignment of the deformed martensite microstructure. Further, crack propagation under ~90° to the surface into the material with a slight diversion towards the direction of the tangential force is detected. The cracks show some branches and arrest at the WEL/BEL interface (Fig. 10b, c). Within the WEL the crack exhibits branches (Fig. 10c), but the crack tip itself is almost blunted. This indicates that the region around the crack tip (being within the BEL) is prone for an increased fracture toughness (Fig. 10d).

Multiple macroscopic cracks initiated within the first ~500 μm of the WEL at the leading edge of the SSL (Fig. 11a) enters the next stage, named *Stage III*. Investigations show that some cracks propagated to the WEL/BEL interface, where they branch. Two major crack-branches are identified: One crack-branch propagates along the WEL/BEL interface along the tangential force, the other in the opposite direction into the BEL (Fig. 11b). Taking a closer look at the crack tips of these two
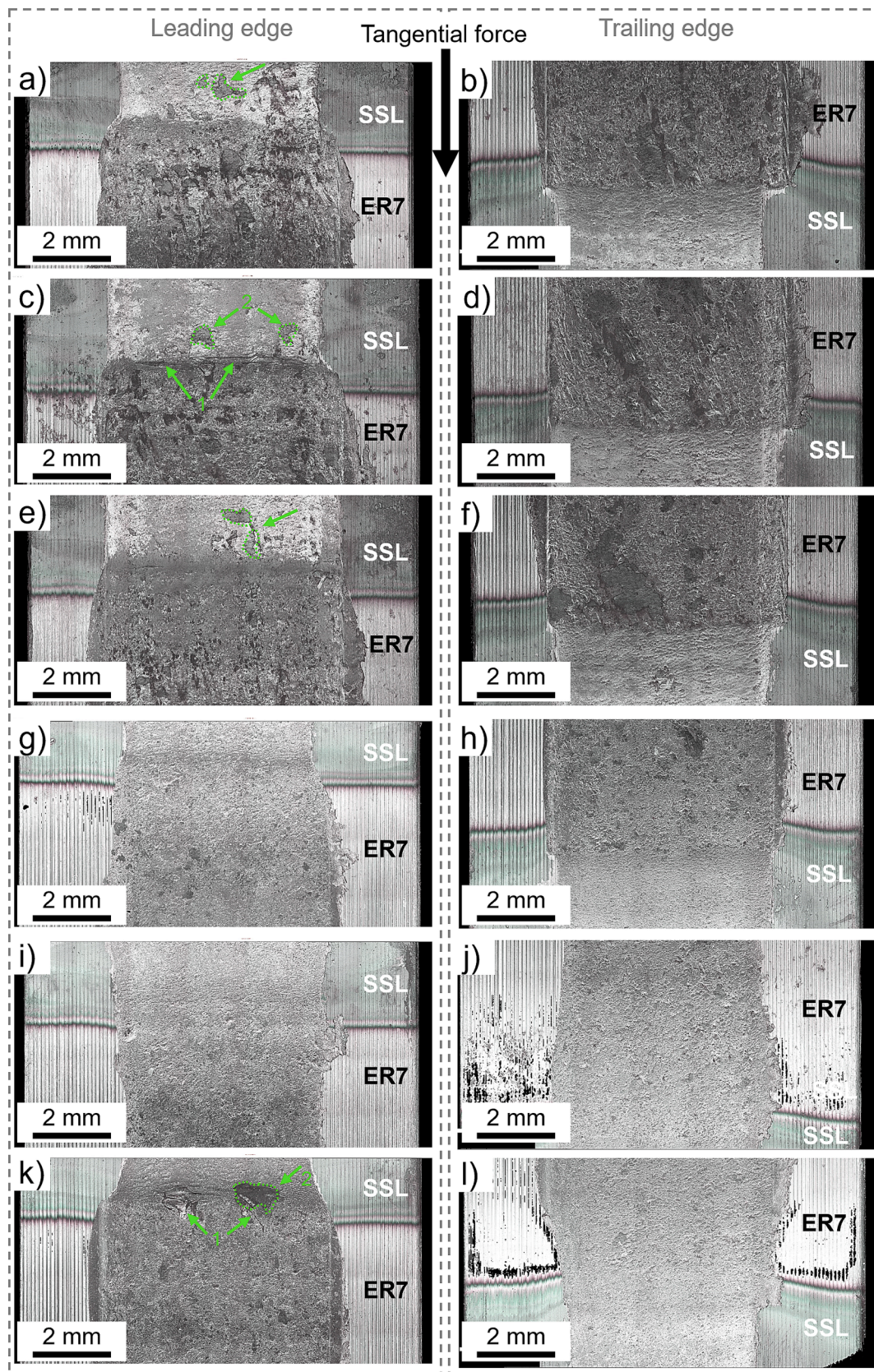
Fig. 6. Surface images (focus-variation microscope) at the transition regions of the run ER7 wheels. Leading edges of the SSLs show crack initiation at the interface (1) for some samples and breakouts of SSL fragments (2). The trailing edges do not show significant damage patterns at the interfaces.
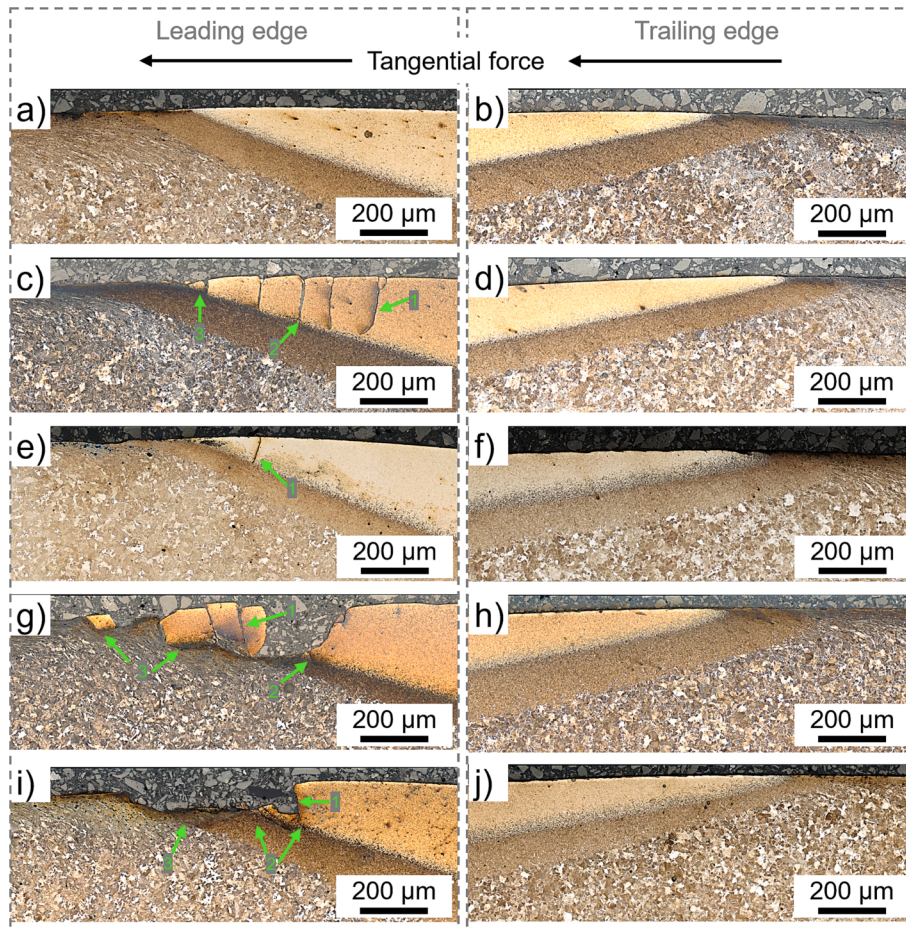
Fig. 7. LOM images of the transition zones from base material to SSLs in cross-sectional cuts for wheel material ER9. The leading edges of the SSLs show failure patterns for 4/5 transition zones: Crack initiation and propagation under 90° to surface within the WEL (1), branching at the WEL/BEL interface (2), and deformation of the BEL due to WEL fragments (3). For the trailing edge, no cracking patterns are detected, but plastic material flow of the base material over the WEL region.

branches shows a sharp crack tip in the WEL/BEL interface (Fig. 11c), contrary to the blunted crack tip present in the BEL (Fig. 11d). This, in combination with the increased length of the crack-branches within the WEL/BEL interface, indicates a faster crack growth there.

The final stage, *Stage IV*, represents fatigue damage of an SSL where significant spallation at the leading edge occurs. This results in a significant geometrical deviation on the wheel surface which can cause a considerable dynamic impact promoting further degradation (Fig. 12a). In *Stage IV*, the crack-branches generated in *Stage III* grow together which leads to the fragmentation of the WEL. Due to the contact situation, the fragments are pushed towards the direction of the tangential and normal forces onto the underlying BEL. This results in a severe deformation of the BEL region (Fig. 12b). Although some WEL fragments already spalled (Fig. 12c), the results and discussions presented above suggest that the cracks branched at the WEL/BEL interface, propagated into the BEL, and arrests there.

Regarding the trailing edges of the SSLs no different stages of fatigue mechanisms are observed (Fig. 5 and Fig. 7). Based on the tangential force pointing towards the SSL edge the material flow seems to strengthen the trailing edge of the SSL. In contrast to the leading edge, the supporting effect of the deformed material hinders macroscopic crack growth. Hence, only wear-related micro-cracks along the WEL surface are present (Fig. 13a). The results further suggest that these cracks are not crucial for the fatigue damage. In some cases, the crack growth direction bends towards the surface leading to the formation of small debris (Fig. 13b). The plastic flow of the BEL and the deformed ferritic-pearlitic microstructure in direction of the tangential force leads

to cavities in the near-surface microstructure (Fig. 13a, c, d). In one case, the more ductile BEL microstructure is sheared over the WEL microstructure and a crack, initiated within the WEL, propagates up to 150 μm along the interface of the WEL and the sheared material (Fig. 13d). Since the crack arrests in the BEL, there is no critical crack propagation leading to significant formation of fragments that would spall.

The change of the surface geometry at the leading edges of the SSLs for the different stages described above is shown by topographical analysis of representative samples in Fig. 14. At *Stage I* and *II* (Fig. 14a and b) no change within the surface can be identified. In contrast, multiple cracks can be seen at *Stage III* (Fig. 14c). Further, at *Stage IV*, a large area with massive spallation within the SSL are present (Fig. 14d).

Based on the results of the analysis so far, a schematic overview of the explanatory model of fatigue crack initiation of SSLs on rail wheel materials is presented in Fig. 15.

3.4. Differences in fatigue crack initiation and propagation with respect to different wheel materials

Based on the results presented *Stage III* is critical for the initiation of fatigue failure of SSLs, since at this stage the smaller fatigue cracks join and result in massive spallation of WEL fragments. Clearly, a difference in degree of damage can be observed between the wheel grades ER7 and ER9 (Fig. 5 and Fig. 7). To understand fatigue crack morphology the evaluation of mechanical properties within the evolved layers is needed, only possible by small-scale testing methods. Therefore, distinctive regions within the SSLs of both wheel materials are further characterized
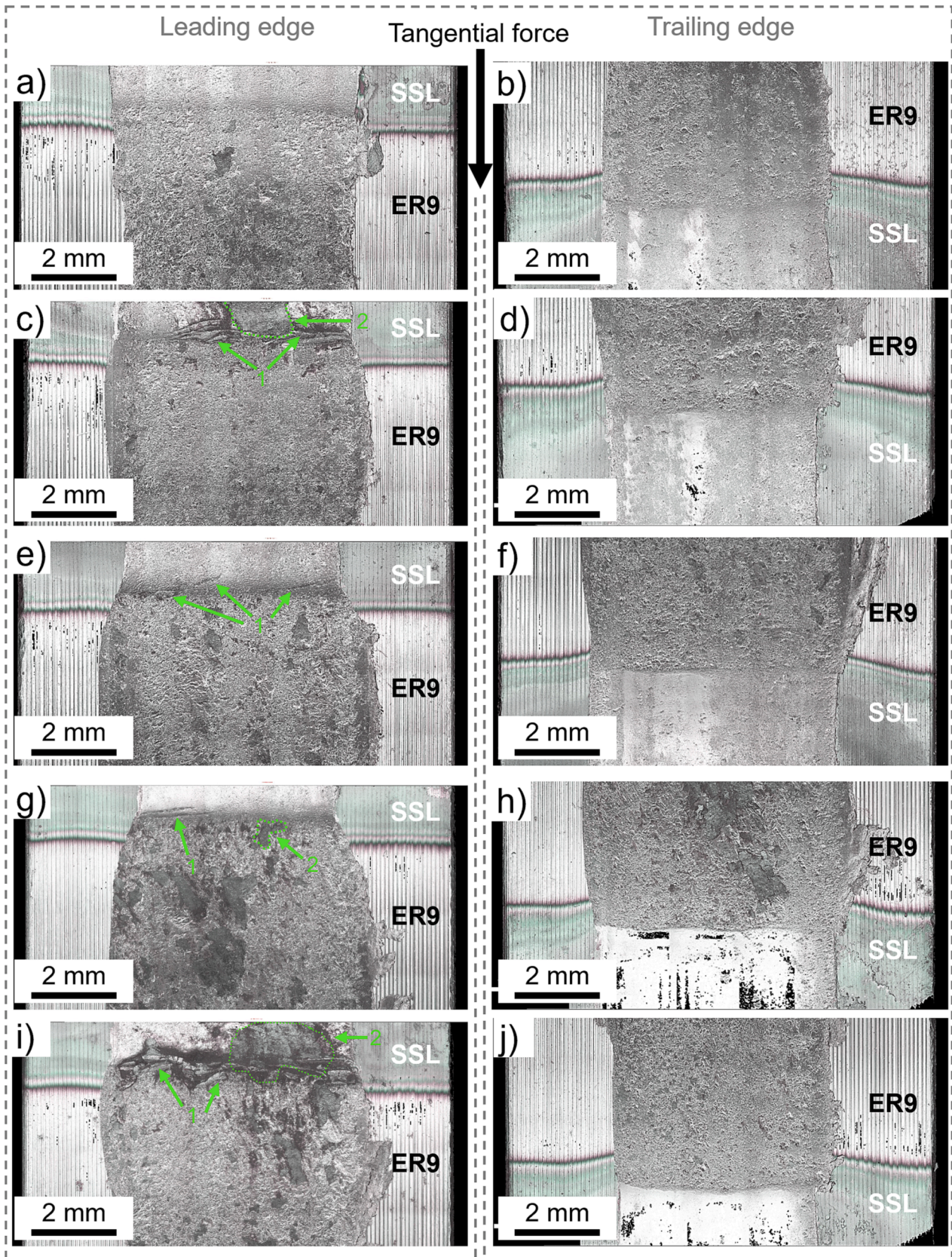
Fig. 8. Surface images (focus-variation microscope) at the transition regions of the run ER9 wheels. The leading edges of the SSLs show crack initiation at the interface (1) for 5 out of 6, in some cases massive breakouts of SSL fragments (2) can be detected. In contrast, the trailing edges do not show significant damage patterns at the interfaces.
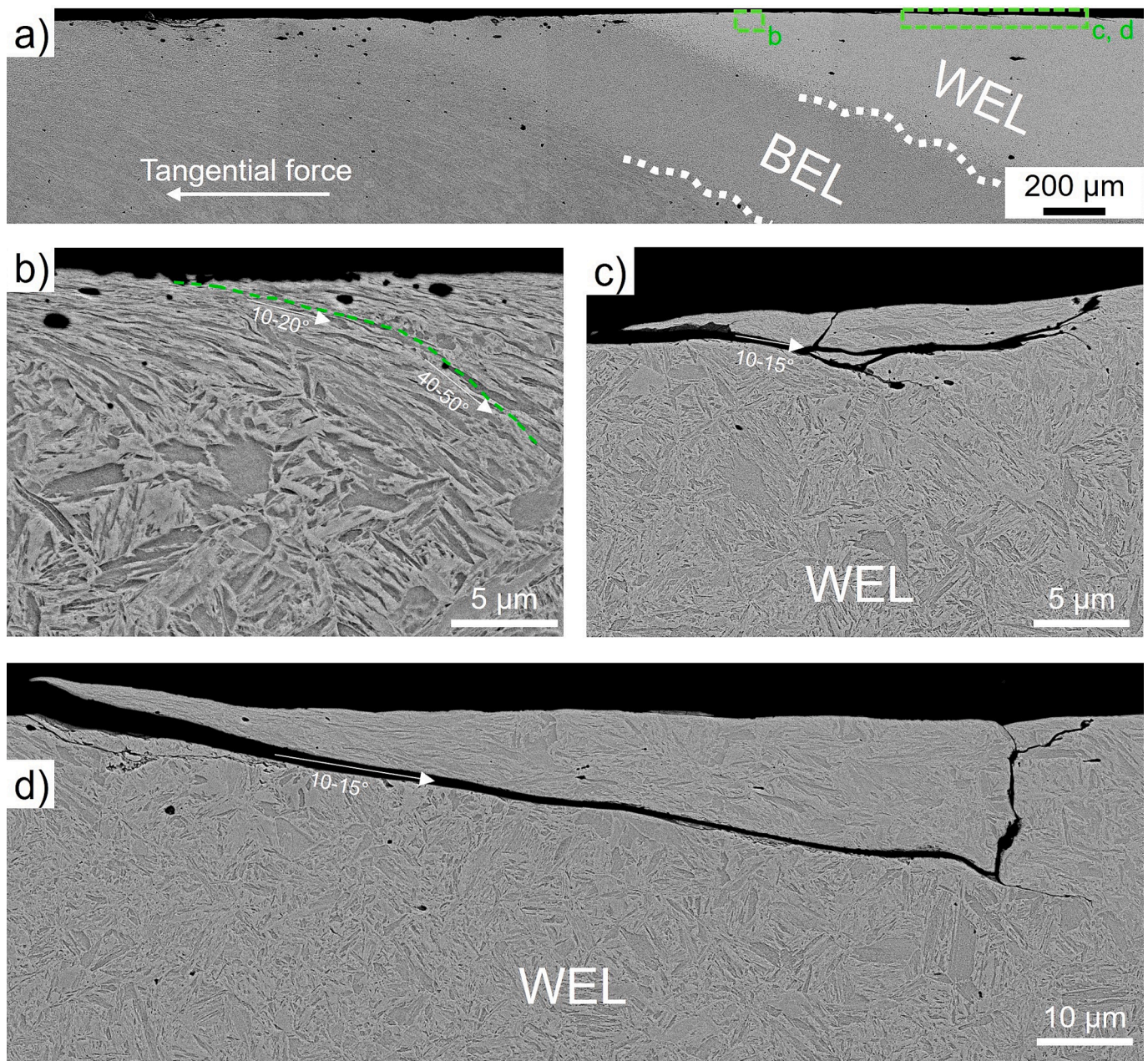
Fig. 9. BE images of the leading edge of the SSL at *Stage I*: (a) No crack initiation within the transition zone of the SSL and the deformed wheel base material. (b) shows the plastic deformation of the WEL within ~20 μm from surface and the alignment of the martensite microstructure. Micro-crack initiation occurs along the WEL surface, cracks under shallow angles (10–15° to the surface) either changing their direction towards the surface (c) or branch and propagate towards the surface (d). In both cases, detachment of wear debris is the result.

by microhardness measurements (Fig. 16a and b). The different regions at the cross sections around the WEL and BEL boarders, Fig. 16a and b, show pronounced differences in Vickers hardness. In addition to hardness, the local fracture toughness K_Q is commonly used to get a sense of potential RCF crack initiation risk in wheel and rail materials [36-38]. Since small-scale fracture toughness experiments would go beyond the scope of the current work, K_Q is estimated according to [38] within this section as follows:

$$K_Q = \frac{A}{HV^B} \tag{2}$$

with microhardness *HV*, and fitting constants *A* = 15,600 MPam$^{1/2}$ and *B* = 1.0. For easier comparison and correlation, these data are presented directly within Fig. 16c. The martensitic WEL regions provide highest

hardness (thus lowest K_Q) of 942 ± 18 and 998 ± 25 HV0.01, see ER7-1 and ER9-1. Within these regions the crack propagates almost perpendicular from the surface towards the WEL/BEL interface, where it is deflected. There, the HV0.01 values are only 587 ± 9 (504 ± 8) and 754 ± 15 (533 ± 9), see ER7-2 (ER7-3) and ER9-2 (ER9-3). In general, the individual regions of ER7 are softer than the corresponding ones of ER9. This is supposed to originate on the higher carbon content of ER9, however, this is not clearly understood so far due to the controversially proposed formation mechanisms of BELs. If we use the common estimation of fracture toughness through the inverse relation with hardness mentioned above, results suggest the lowest fracture toughness within the WEL and a trend of higher fracture toughness values for SSL regions of the ER7 wheel material.
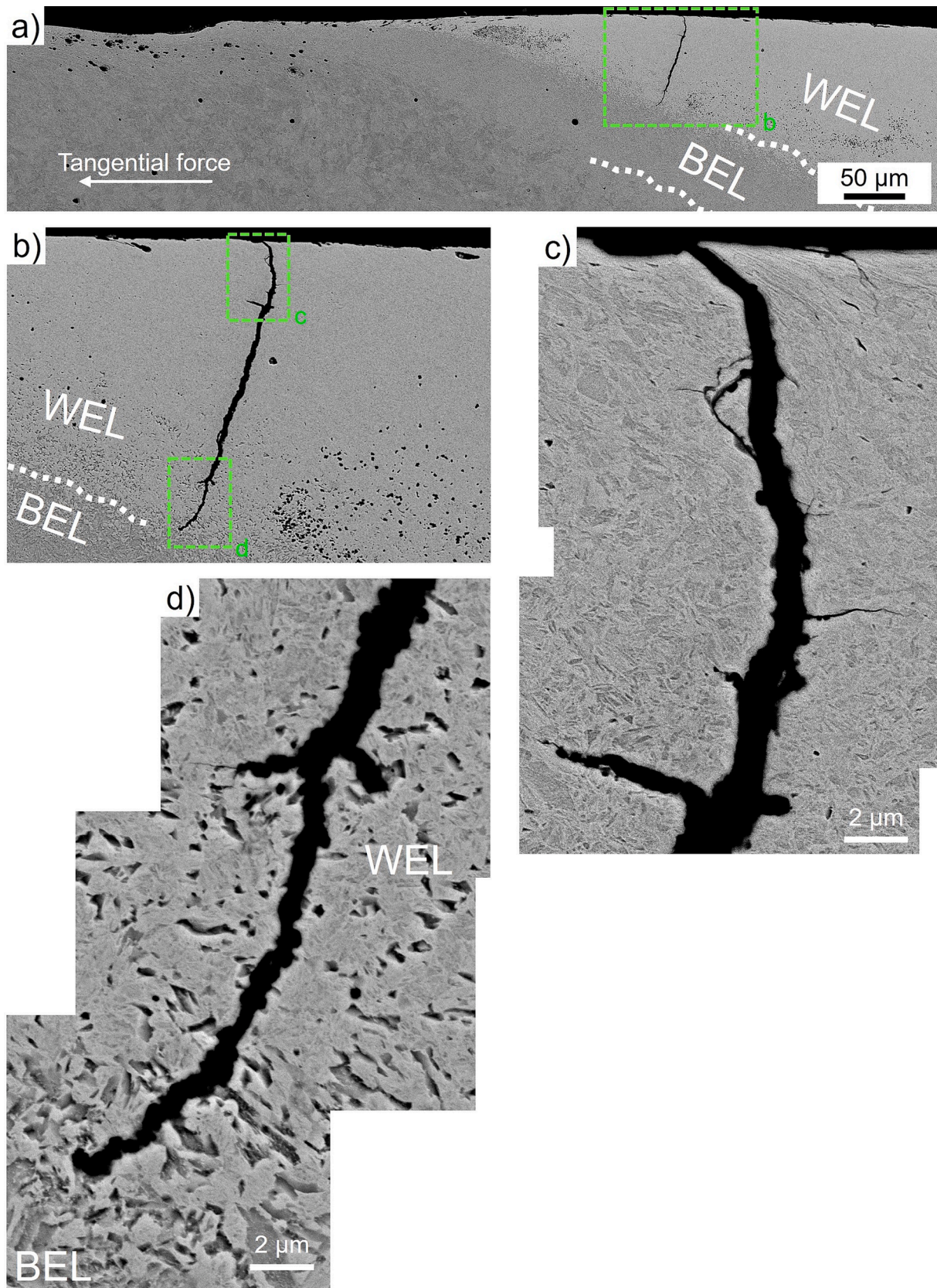
Fig. 10. BE images of the leading edge of the SSL at *Stage II* are characterized by macroscopic crack initiation at the WEL with crack propagation ~90° to the surface down to the WEL/BEL interface (a), (b). The crack first propagates along the deformed martensitic microstructure (c), the crack tip is situated just in the BEL region and shows significant blunting (d).
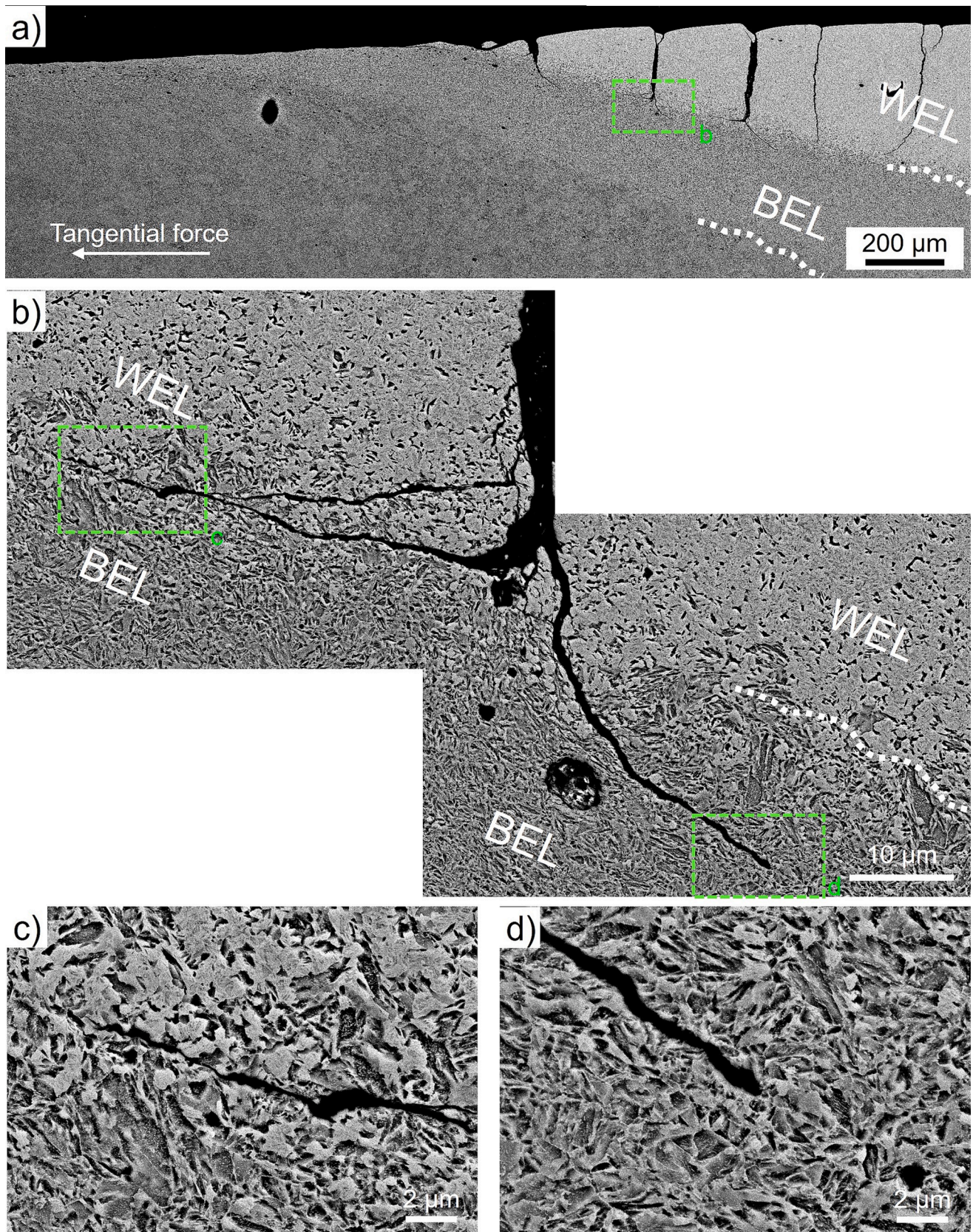
Fig. 11. BE images of the leading edge of the SSL at *Stage III*: Multiple cracks are evident in the WEL next to the transition zone (a), with crack branching at the WEL/BEL interface (b). One crack branch propagates along the WEL/BEL interface in direction of the tangential force and is characterized by a sharp crack tip (c), the other propagates into the BEL showing a minor crack length and a blunt crack tip (d).
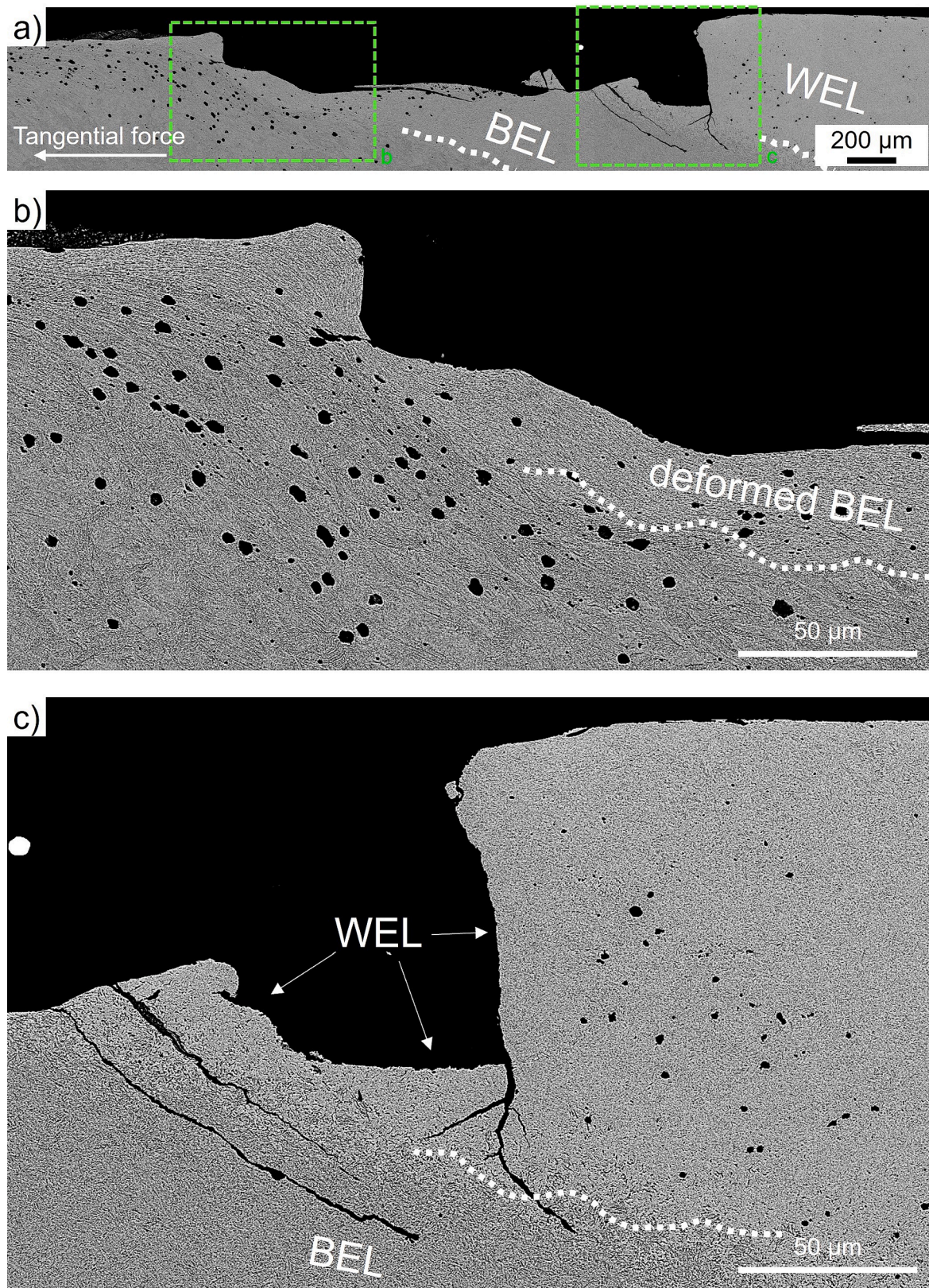
Fig. 12. BE images of the leading edge of the SSL at the final stage, *Stage IV*. This stage comes up with a massive geometrical deviation on the wheel surface due to spallation of WEL fragments (a). The cracks branched at the WEL/BEL interface in Stage III merge and WEL fragments are spalled, pushed towards the direction of the tangential and normal forces against the underlying BEL and leading to a severe deformation of the BEL (b). The branched cracks propagating into the BEL are still existing, but further propagation is not expected (c).
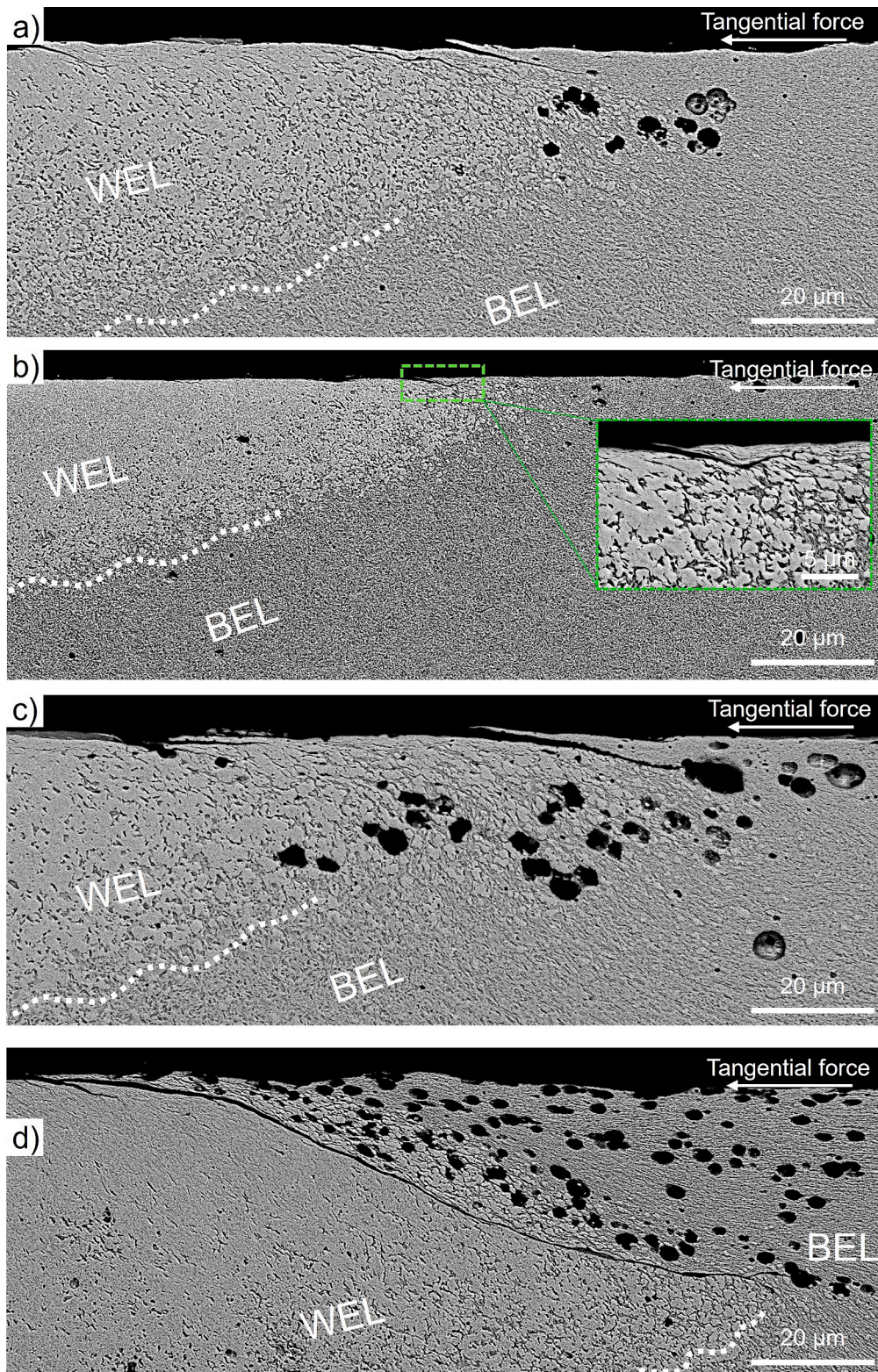
Fig. 13. BE images of the trailing edges of the SSLs, which do not show critical crack initiation, but material flow of the BEL and wheel base material in the direction of the tangential force. Wear dominated micro-cracks can be identified along the WEL surface (a), propagating towards the surface in most cases (b), or stopping at cavities (c). Massive material flow leads to formation of cavities, where, in one case (d), a crack propagated along the transition to the WEL.

4. Discussion

The major drawback when investigating wheel and rail samples from the field is their unknown loading history. But for detailed fatigue investigations, well-defined and known conditions are needed to draw reasonable conclusions. Therefore, the wheel and rail sample materials were well-defined treated with the help of a twin disc tribometer in our laboratory. The conditions of the field operations are mimicked by a mechanical load (to deform the material) followed by two thermal loads, which finally form WEL and BEL layers (being similar to the field
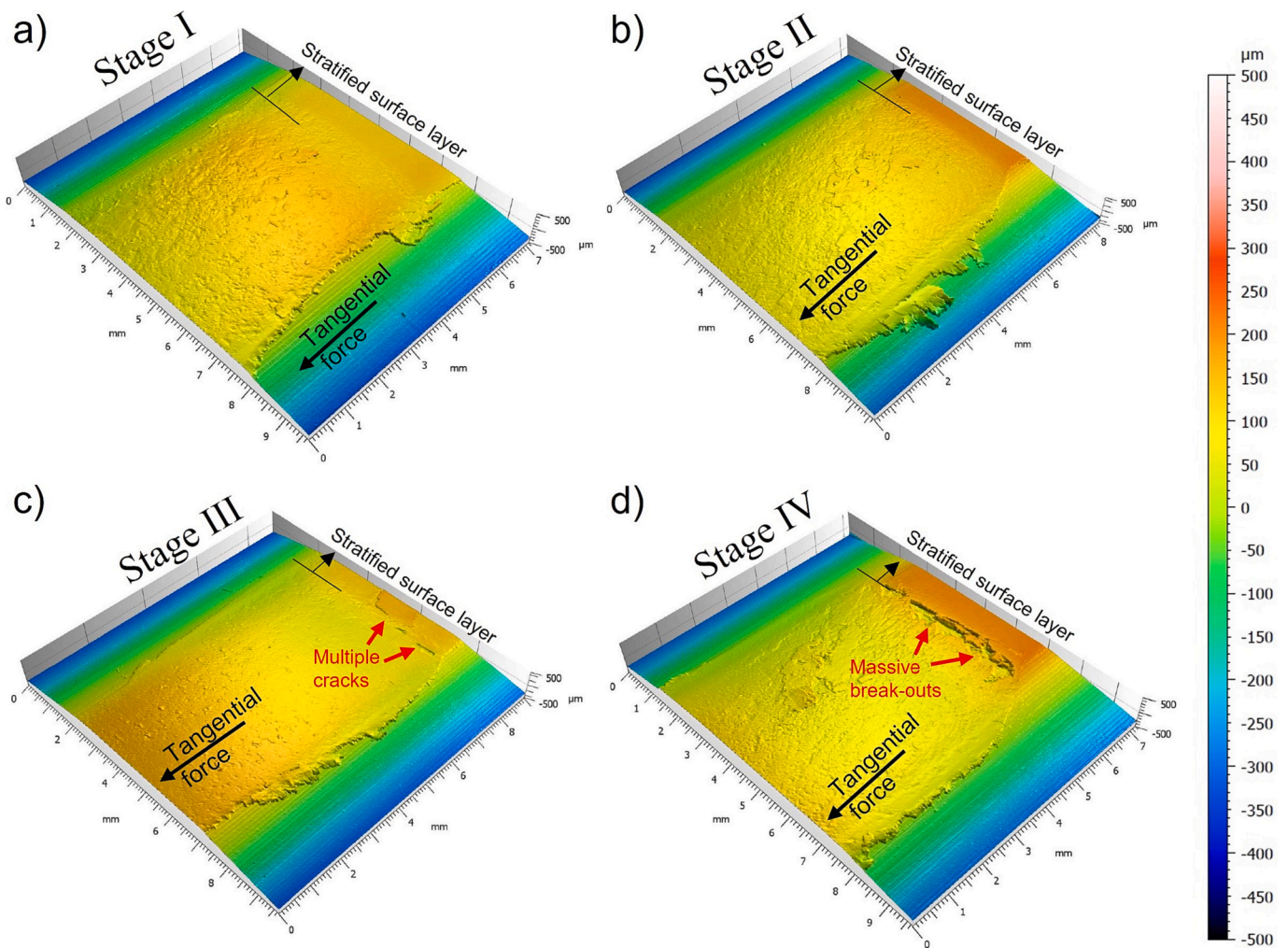
Fig. 14. Topographical analysis of representative leading edges of the SSLs: *Stage I* (a) and *II* (b) do not show significant changes at the surface, in contrast, at *Stage III* (c) multiple cracks can be identified. At the final stage, *Stage IV* (d) massive spallation within the SSL can be seen, leading to significant geometrical changes of the discs.

samples). These disc samples were afterwards mechanically treated to initiate fatigue damages.

Due to surface inhomogeneities as a result of the first mechanical loading, the laser parameters, based on our previous work [14], where slightly changed for having a pre-defined output power. This guarantees the targeted surface temperature based on a comparable coefficient of absorption for the wheel steel samples within this work. Thus, the first thermal load (T1) was performed with a laser energy of P = 4 kW (which corresponds to an energy input of ~3.5 Ws/mm^2), resulting in an estimated surface temperature of ~930 °C. This is in the range of possible temperatures reached for wheel–rail contacts [17] and above the austenitization temperature of the wheel steels. Initial trails showed that only a second thermal load (T2) with less laser energy compared to the first leads to the formation of a BEL layer. The selected laser power of P = 3.2 kW induced a pronounced BEL consisting of tempered martensite microstructure underneath the martensitic WEL. This is in accordance with one proposed formation mechanism of BEL (Route 2) by Kumar et al. [28]. Further, the microstructure of the BEL created in the current work corresponds to the tempered martensite stated in [29] and former works from the authors [39,40]. In contrast, the presented approach to create SSLs contradicts the proposed formation mechanism by Messadi et al. [30] where a single thermal loading is suggested to create a martensitic WEL with a bainitic BEL underneath.

The novel experimental approach of combining twin disc testing and surface laser treatment was successful in creating plastic shear deformation and WEL and BEL layers at the surface, as well as crack initiation and crack propagation in good correlation with reports from field samples [41]. The results obtained here are in agreement with results reported in literature using a twin disc tribometer to investigate the crack behavior of WELs, either created by rolling-sliding friction tests [22,42] or laser discrete quenching (LDQ) [43,44] on rail materials. Seo et al. [22] reported two types of cracks, one between the WEL and the undeformed area underneath, the other at the center of the WEL. The branching observed at the end of the WEL resembles the branching at the WEL/BEL interface at *Stage III* within our work. The vertical strip-shape LDQ tested in the work of Ding et al. [43] also reveals similarities to the laser surface treatments of our work. Crack initiation and propagation with large angles could be observed in the edge of the quenching region, explained by the high hardness of the martensite and the relatively low strength and less supporting effect of the underlying material due to decreasing thickness at the edges. Crack branching at the end of the WEL was shown, where cracks either propagate into the substrate or along the boundary [43]. Studies with respect to crack initiation in the presence of WELs were commonly published on rail samples from field, as shown by Steenbergen et al. [8] and Al-Juboori et al. [45], where the cracks initiate at the transition zone of the WEL and the rail material. Especially the border regions of the WEL to the base material or the BEL are sensitive regions for the crack propagation, as our results show. The sudden change in microhardness causes the cracks (running from the WEL regions) to deflect and branch, which consumes energy and would be an
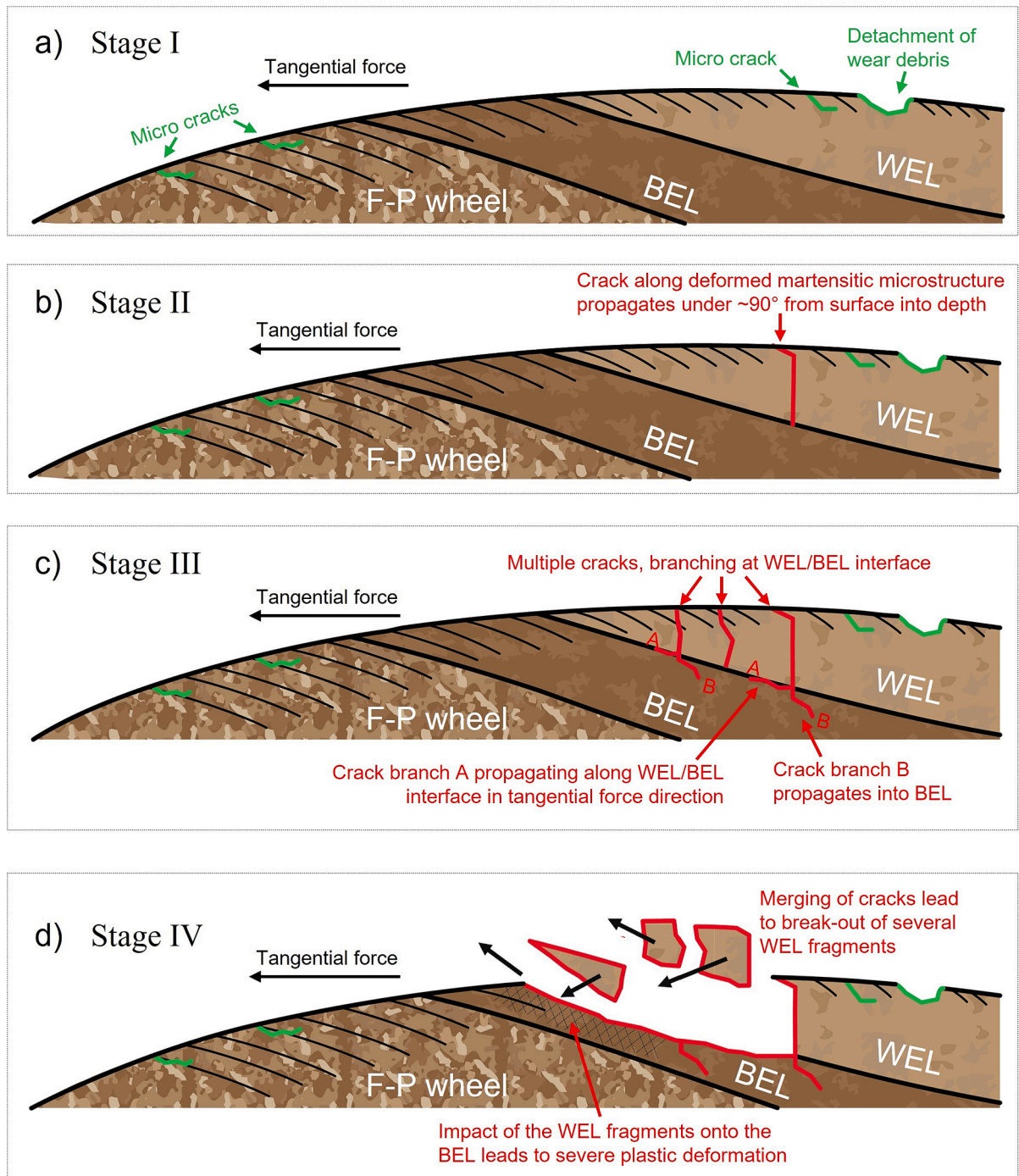
Fig. 15. Explanatory model of fatigue crack initiation at the leading edges of SSLs on wheel materials: The wear dominated *Stage I* (a) shows no macroscopic crack in the transition zone of the ferritic-pearlitic wheel material (F-P wheel), to the BEL and the WEL. The depth of plastic deformation is decreasing with increasing hardness (F-P wheel → BEL → WEL). Micro-cracks can be observed along the disc surface, stopping, or turning towards the surface resulting in detachment of wear debris. At *Stage II* (b) a vertical crack is initiated within the WEL next to the transition zone. Initiated at the surface, the crack first propagates along the aligned martensite grains and further under ~90° from surface into depth until the WEL/BEL interface. *Stage III* is representing multiple cracks initiated within the WEL near the transition zone, with branching occurring at the WEL/BEL interface. One crack branch (A) propagates along the WEL/BEL interface in the direction of the tangential force, the other (B) in opposite direction downwards into the BEL. Finally, at *Stage IV*, the crack branches merge and fragments of the WEL break out. At least some WEL fragments get pushed against the underlying BEL, leading to a severe plastic deformation of the BEL.

advantage to reduce the crack propagation. But this unfortunately also lead to chipping-off of some WEL or BEL material (Fig. 9). Our results about the branching characteristics of the cracks at the boundaries of the WEL to the underlying rail material are in agreement with reports of Pereira et al. [46], about RCF on ex-service rails with detected WELs. They actually suggested that the microstructural heterogeneity

promotes the change in crack growth directions. Österle et al. [47] further showed that within the WEL regions on rails high compressive residual stresses are present, which originate from phase transformations and the connected volume expansion. Additionally, Lian et al. [48] proposed (based on FE-modelling) that residual stresses within the WEL also change due to multiple train passages (thus loading
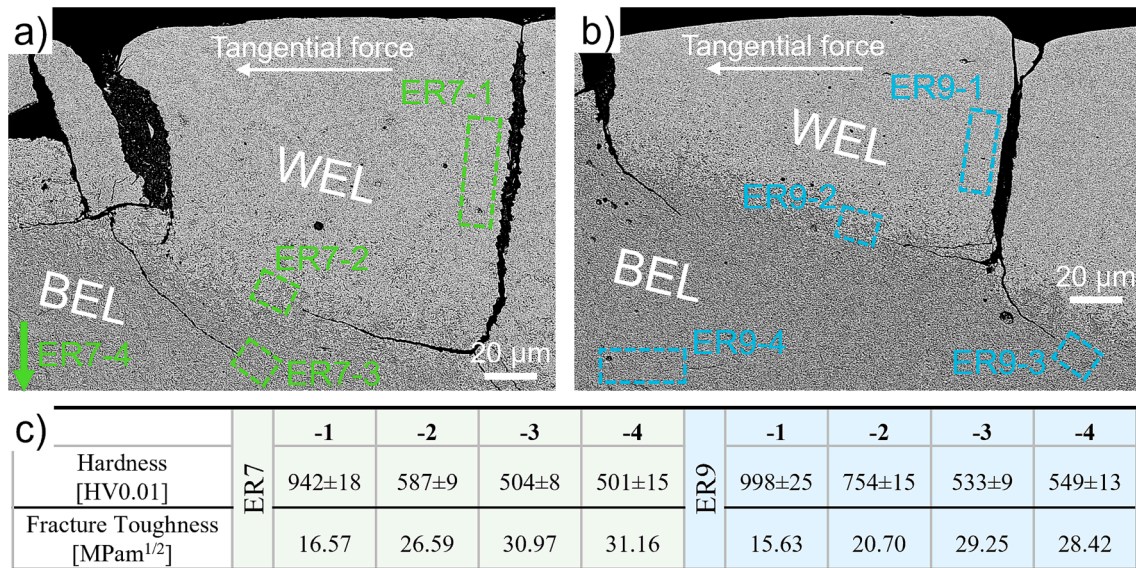
Fig. 16. Microhardness measurements are conducted in specific regions at the leading edge of SSL at *Stage III* on the (a) ER7 wheel steel, and (b) ER9 wheel steel. The obtained hardness values and the estimated local fracture toughness values are given in (c).

changes). Earlier, the same authors highlighted (also based on numerical models) that when the wheel passes from the rail matrix to the WEL, the normal contact stress sharply increases [49], contributing to the crack initiation observed in the wheel materials here, where the most critical cracks (largest ones) are present within the WEL itself. Due to a volume reduction during tempering of martensite, high residual stresses build up, promoting fatigue crack initiation [50]. Although the tempered martensite may correspond to the BEL of our study, the fatigue crack initiation is different. Additionally to the crack initiation at the borders of the WEL, Li et al. [27] and Messadi et al. [30] also showed that cracks are initiated within the BEL of SSLs on rails. This can be due to the higher loads present during real field operations and additional dynamic effects. However, our studies ensure defined loading parameters (mechanical and thermal) in both for the formation of the SSLs and the fatigue testing. This paves the way for future systematic studies, where different influencing parameters can be studied and fundamental knowledge about RCF in the presence of SSLs can be gained. In terms of influencing parameters, the material properties play a crucial role with respect to fatigue crack initiation and propagation. In this study, two wheel materials, ER7 and ER9, are investigated with equal preceding heat treatment. Results indicate clear differences in their crack propagation and deflection, compare Fig. 5 and Fig. 7. The sensitivity for crack initiation and propagation of the ER9 wheel material can be rationalized with their typically higher microhardness values, Fig. 16. However, determination of further mechanical properties such as fatigue strength is hampered due to the small scale of the evolved layers. Thus, efforts have been made by applying small-scale testing techniques to evaluate the local fracture toughness with high spatial resolution of wheel and rail materials [36-38,51]. To not exceed the framework within the current study, a common estimation of the local fracture toughness was used, showing a good comparability to results conducted for samples from the field. Moreover, findings in the presented work will act as a useful reference to future microstructural and micro-mechanical characterizations of SSLs on wheel and rail near-surface microstructures and their fatigue crack morphologies.

5. Conclusions

The main conclusions of the presented study on fatigue crack initiation of SSLs (WEL + BEL) on different wheel materials created by defined mechanical and thermal loads are:

- The established laboratory approach to create reproducible SSLs on wheel steels shows a good comparability to wheels from field. The combination of a twin disc tribometer and laser surface treatments mimics an SSL with defined mechanical and thermal loading parameters.
- The fatigue tests of the SSLs show different degrees of fatigue crack initiation and propagation exclusively on the leading edge of the SSL.
- The material ER9 (higher microhardness and lower estimated local fracture toughness in the surrounding areas of the identified cracks) showed more extensive fatigue crack initiation and propagation.

The results obtained, allow to derive an explanatory four-stage model of fatigue crack initiation at the leading edges of the SSLs. Within *Stage I* no fatigue cracks initiate, but wear-related micro-cracks along the WEL surface. At *Stage II* a macroscopic crack initiates in the WEL next to the transition to the deformed wheel material, propagating ~90° to the surface towards the WEL/BEL interface. *Stage III* is dominated by multiple crack initiation (analogous to *Stage II*), which further branch at the WEL/BEL interface. One crack-branch propagates along the WEL/BEL interface in the direction of the tangential force, the other in the opposite direction downwards into the BEL at a slower crack growth rate. In *Stage IV*, several crack-branches grow together, causing significant spallation of material above them. The trailing edges of the SSLs do not show fatigue crack formation, which is explained by the supporting effect of the underlying material and the plastic material flow towards the SSL in tangential force direction.

The presented systematic study of SSLs created under defined mechanical and thermal loads points out their relation to fatigue crack initiation and propagation of rail wheels in service.

CRediT authorship contribution statement

M. Freisinger: Conceptualization, Methodology, Validation, Data curation, Writing – original draft. **B. Jakab:** Data curation, Writing – review & editing. **K. Pichelbauer:** Data curation, Writing – review & editing. **G. Trummer:** Supervision, Writing – review & editing. **K. Six:** Supervision, Writing – review & editing. **P. Mayrhofer:** Supervision, Writing – review & editing.

Declaration of Competing Interest

The authors declare that they have no known competing financial interests or personal relationships that could have appeared to influence the work reported in this paper.

Data availability

Data will be made available on request.

Acknowledgments

References

[1] Andersson R, Ahlström J, Kabo E, Larsson F, Ekberg A. Numerical investigation of crack initiation in rails and wheels affected by martensite spots. Int J Fatigue 2018;114:238–51. https://doi.org/10.1016/j.ijfatigue.2018.05.023.

[2] Ekberg A, Åkesson B, Kabo E. Wheel/rail rolling contact fatigue – Probe, predict, prevent. Wear 2014;314(1–2):2–12. https://doi.org/10.1016/j.wear.2013.12.004.

[3] Ekberg A, Kabo E. Fatigue of railway wheels and rails under rolling contact and thermal loading—an overview. Wear 2005;258(7–8):1288–300. https://doi.org/10.1016/j.wear.2004.03.039.

[4] Zhang SY, et al. Rail rolling contact fatigue formation and evolution with surface defects. Int J Fatigue 2022;158:106762. https://doi.org/10.1016/j.ijfatigue.2022.106762.

[5] Liu Y, Stratman B, Mahadevan S. Fatigue crack initiation life prediction of railroad wheels. Int J Fatigue 2006;28(7):747–56. https://doi.org/10.1016/j.ijfatigue.2005.09.007.

[6] Peixoto DFC, de Castro PMST. Fatigue crack growth of a railway wheel. Eng Fail Anal 2017;82:420–34. https://doi.org/10.1016/j.engfailanal.2017.07.036.

[7] Grassie SL. Studs and squats: The evolving story. Wear 2016;366–367:194–9. https://doi.org/10.1016/j.wear.2016.03.021.

[8] Steenbergen M. Squat formation and rolling contact fatigue in curved rail track. Eng Fract Mech 2015;143:80–96. https://doi.org/10.1016/j.engfracmech.2015.05.060.

[9] Steenbergen M. On the genesis of squat-type defects on rails – Toward a unified explanation. Wear 2021;478–479:203906. https://doi.org/10.1016/j.wear.2021.203906.

[10] Grassie SL. Squats and squat-type defects in rails: the understanding to date. Proceedings of the Institution of Mechanical Engineers, Part F: Journal of Rail and Rapid Transit 2012;226(3):235–42. https://doi.org/10.1177/0954409711422189.

[11] Grassie SL, Fletcher DI, Gallardo Hernandez EA, Summers P. Studs: a squat-type defect in rails. Proceedings of the Institution of Mechanical Engineers, Part F: Journal of Rail and Rapid Transit 2012;226(3):243–56. https://doi.org/10.1177/0954409711421462.

[12] Hieu Nguyen B, Al-Juboori A, Zhu H, Zhu Q, Li H, Tieu K. Formation Mechanism and Evolution of White Etching Layers on Different Rail Grades. Int J Fatigue 2022:107100. https://doi.org/10.1016/j.ijfatigue.2022.107100.

[13] Al-Juboori A, et al. Characterisation of White Etching Layers formed on rails subjected to different traffic conditions. Wear 2019;436–437:202998. https://doi.org/10.1016/j.wear.2019.202998.

[14] Freisinger M, et al. Comparative study on the influence of initial deformation and temperature of thermally induced white etching layers on rail wheels. Tribol Int 2023;177:107990. https://doi.org/10.1016/j.triboint.2022.107990.

[15] Pan R, Chen Y, Lan H, E S, Ren R. Investigation into the evolution of tribological white etching layers. Mater Charact 2022;190:112076. https://doi.org/10.1016/j.matchar.2022.112076.

[16] Carroll RI, Beynon JH. Rolling contact fatigue of white etching layer: Part 1 Crack morphology. Wear 2007;262:1253–66. https://doi.org/10.1016/j.wear.2007.01.003.

[17] Bernsteiner C, et al. Simulation and experiment based investigations of squat formation mechanisms. Wear 2019;440–441:203093. https://doi.org/10.1016/j.wear.2019.203093.

[18] Pan R, Ren R, Chen C, Zhao X. The microstructure analysis of white etching layer on treads of rails. Eng Fail Anal 2017;82:39–46. https://doi.org/10.1016/j.engfailanal.2017.06.018.

[19] Farjoo M, Daniel W, Meehan PA. Modelling a squat form crack on a rail laid on an elastic foundation. Eng Fract Mech 2012;85:47–58. https://doi.org/10.1016/j.engfracmech.2012.02.004.

[20] Lian Q, et al. Crack propagation behavior in white etching layer on rail steel surface. Eng Fail Anal 2019;104:816–29. https://doi.org/10.1016/j.engfailanal.2019.06.067.

[21] Pal S, Daniel WJT, Farjoo M. Early stages of rail squat formation and the role of a white etching layer. Int J Fatigue 2013;52:144–56. https://doi.org/10.1016/j.ijfatigue.2013.02.016.

[22] Seo J, Kwon S, Jun H, Lee D. Numerical stress analysis and rolling contact fatigue of White Etching Layer on rail steel. Int J Fatigue 2011;33(2):203–11. https://doi.org/10.1016/j.ijfatigue.2010.08.007.

[23] Deuce R. Wheel Tread Damage - An Elementary Guide. Bombardier Transportation GmbH, Netphen, Germany, Technical Report; 2007.

[24] Liu C, et al. Formation mechanism for the white etching microstructure in the subsurface of the failure pearlite wheel steel. Wear 2022;494–495:204243. https://doi.org/10.1016/j.wear.2022.204243.

[25] Zhang YM, Xiao ZM, Fan M. Fatigue Investigation on Railway Wheel Steel with White Etching Layer. Int J Steel Struct 2020;20(1):80–8. https://doi.org/10.1007/s13296-019-00271-x.

[26] Kato T, Sugeta A, Nakayama E. Investigation of influence of white layer geometry on spalling property in railway wheel steel. Wear 2011;271(1–2):400–7. https://doi.org/10.1016/j.wear.2010.10.024.

[27] Li S, Wu J, Petrov RH, Li Z, Dollevoet R, Sietsma J. "Brown etching layer": A possible new insight into the crack initiation of rolling contact fatigue in rail steels? Eng Fail Anal 2016;66:8–18. https://doi.org/10.1016/j.engfailanal.2016.03.019.

[28] Kumar A, Agarwal G, Petrov R, Goto S, Sietsma J, Herbig M. Microstructural evolution of white and brown etching layers in pearlitic rail steels. Acta Materialia 2019;171:48–64. https://doi.org/10.1016/j.actamat.2019.04.012.

[29] Tung P-Y, Zhou X, Morsdorf L, Herbig M. Formation mechanism of brown etching layers in pearlitic rail steel. Materialia 2022;26:101625. https://doi.org/10.1016/j.mtla.2022.101625.

[30] Messaadi M, Steenbergen M. Stratified surface layers on rails. Wear 2018;414–415:151–62. https://doi.org/10.1016/j.wear.2018.07.019.

[31] Ahlstrom J, Karlsson B. Microstructural evaluation and interpretation of the mechanically and thermally affected zone under railway wheel flats. Wear 1999:14.

[32] Lagerberg G, A J. Influence of grain boundaries on the behaviour of carbon and nitrogen in α-iron. Acta Metall 1955;3(3):236–44.

[33] 'EN 13262:2004+A2:2011: Railway applications - Wheelsets and bogies - Wheels - Product requirements'.

[34] Herian J, Aniołek K. Abrasive wear of railway sections of steel with a different pearlite morphology in railroad switches. J Achievements Mater Manuf Eng, 2010;43.

[35] Diener M, Ghidini A. Fracture Toughness: A Quality Index for Railway Solid Wheels. Matls Perf Charact 2014;3(3):20130047. https://doi.org/10.1520/MPC20130047.

[36] Kumar A, et al. In situ study on fracture behaviour of white etching layers formed on rails. Acta Materialia 2019;180:60–72. https://doi.org/10.1016/j.actamat.2019.08.060.

[37] Freisinger M, Zauner L, Hahn R, Riedl H, Mayrhofer PH. In-situ micro-cantilever bending studies of a white etching layer thermally induced on rail wheels. Mater Sci Eng A 2023;869:144805. https://doi.org/10.1016/j.msea.2023.144805.

[38] Saxena AK, Kumar A, Herbig M, Brinckmann S, Dehm G, Kirchlechner C. Micro fracture investigations of white etching layers. Mater Des 2019;180:107892. https://doi.org/10.1016/j.matdes.2019.107892.

[39] Freisinger M, Rojacz H, Trausmuth A, Mayrhofer PH. Severe Plastic Deformed Zones and White Etching Layers Formed During Service of Railway Wheels. Metallogr Microstruct Anal 2023. https://doi.org/10.1007/s13632-023-00967-x.

[40] Freisinger M, Trausmuth A. Microstructural characterization of near-surface microstructures on rail wheels in service – an insight into "stratified surface layers". Open Res Europe 2023;3:73. https://doi.org/10.12688/openreseurope.15881.1.

[41] Fantecelle Strey N, Bavaresco Rezende A, da Silva Miranda R, Tamara da Fonseca S, Mei PR, Scandian C. Comparison of rolling contact fatigue damage between railway wheels and twin-disc test specimens. Tribol Int 2021;160:107037. https://doi.org/10.1016/j.triboint.2021.107037.

[42] Zhou Y, Mo J, Cai Z, Deng C, Peng J, Zhu M. Third-body and crack behavior in white etching layer induced by sliding–rolling friction. Tribol Int 2019;140:105882. https://doi.org/10.1016/j.triboint.2019.105882.

[43] Ding HH, et al. Investigation on the rolling wear and damage properties of laser discrete quenched rail material with different quenching shapes and patterns. Surf Coat Technol 2019;378:124991. https://doi.org/10.1016/j.surfcoat.2019.124991.

[44] Cao X, Shi LB, Cai ZB, Liu QY, Zhou ZR, Wang WJ. Investigation on the microstructure and damage characteristics of wheel and rail materials subject to laser dispersed quenching. Appl Surf Sci 2018;450:468–83. https://doi.org/10.1016/j.apsusc.2018.04.210.

[45] Al-Juboori A, et al. Squat formation and the occurrence of two distinct classes of white etching layer on the surface of rail steel. Int J Fatigue 2017;104:52–60. https://doi.org/10.1016/j.ijfatigue.2017.07.005.

[46] Pereira JI, Tressia G, Kina EJ, Sinatora A, Souza RM. Analysis of subsurface layer formation on a pearlitic rail under heavy haul conditions: Spalling characterization. Eng Fail Anal 2021;130:105549. https://doi.org/10.1016/j.engfailanal.2021.105549.

[47] Österle W, Rooch H, Pyzalla A, Wang L. Investigation of white etching layers on rails by optical microscopy, electron microscopy, X-ray and synchrotron X-ray diffraction. Mater Sci Eng A 2001;303(1–2):150–7. https://doi.org/10.1016/S0921-5093(00)01842-6.

[48] Lian Q, et al. Evolution of thermally induced white etching layer at rail surface during multiple wheel/train passages. Int J Fatigue 2022;159:106799. https://doi.org/10.1016/j.ijfatigue.2022.106799.

[49] Lian Q, Deng G, Zhu H, Li H, Wang X, Liu Z. Influence of white etching layer on rolling contact behavior at wheel-rail interface. Friction 2020;8(6):1178–96. https://doi.org/10.1007/s40544-020-0388-x.

[50] Esmaeili A, Ahlström J, Andersson B, Ekh M. Modelling of cyclic plasticity and phase transformations during repeated local heating events in rail and wheel steels. Int J Fatigue 2021;151:106361. https://doi.org/10.1016/j.ijfatigue.2021.106361.

[51] Freisinger M, Trausmuth A, Hahn R, Badisch E. Influence of the evolution of near-surface rail wheel microstructure on crack initiation by micro-bending investigations. Proc Inst Mech Eng, Part F: J Rail Rapid Transit, 2023; 09544097231191550, doi: 10.1177/09544097231191550.